



Predicting Progressive Delamination of Composite Material Specimens via Interface Elements

J. Chen, M. Crisfield, A. J. Kinloch, E. P. Busso, F. L. Matthews, Y. Qiu


To cite this article: J. Chen, M. Crisfield, A. J. Kinloch, E. P. Busso, F. L. Matthews, Y. Qiu (1999) Predicting Progressive Delamination of Composite Material Specimens via Interface Elements, Mechanics of Composite Materials and Structures, 6:4, 301-317

To link to this article: <https://doi.org/10.1080/107594199305476>



Published online: 30 Nov 2010.



Submit your article to this journal 



Article views: 494



Citing articles: 97 View citing articles 



Predicting Progressive Delamination of Composite Material Specimens via Interface Elements

J. CHEN

Centre for Composite Materials, Imperial College of Science,
Technology and Medicine, London, United Kingdom

M. CRISFIELD

Department of Aeronautics, Imperial College of Science,
Technology and Medicine, London, United Kingdom

A. J. KINLOCH

E. P. BUSSO

Department of Mechanical Engineering, Imperial College of Science,
Technology and Medicine, London, United Kingdom

F. L. MATTHEWS

Centre for Composite Materials, Imperial College of Science,
Technology and Medicine, London, United Kingdom

Y. QIU

Department of Aeronautics, Imperial College of Science,
Technology and Medicine, London, United Kingdom

ABSTRACT

This article describes the application of interface elements to the prediction of progressive delamination in composite materials. The work has been implemented in two separate commercial finite-element computer packages, ABAQUS [1] and LUSAS [2]. In the former case, this has been achieved via a "user subroutine," while in the latter case the elements are embedded directly within the system, either in the standard "release version" of the code or in a research version, to which the authors have access and in which they have implemented various algorithms directly. Comparisons are made with a range of experimental results for composite material specimens. In addition to the finite-element solutions, closed-form results are also presented that are based on a corrected beam theory.

Traditional methods for predicting interlaminar delamination in composite structures apply fracture mechanics directly, in conjunction with techniques such as the virtual crack closure method [3, 4]. Crack propagation can be simulated by advancing the crack front when the local energy release rate rises to its critical value [5]. To apply such methods, one must

Received 8 October 1998; accepted 25 March 1999.

Address correspondence to J. Chen, Centre for Composite Materials, Department of Aeronautics, Imperial College of Science, Technology and Medicine, Exhibition Road, London SW7, 2BY, UK.

introduce an initial flaw. In contrast to these approaches, we will describe here a method based on the indirect use of fracture mechanics in which a softening decohesion material model is provided with traction/relative displacement relationships that are so constructed that the enclosed area is equated to the critical fracture energy. The solutions are then obtained by a direct application of a nonlinear, finite-element, path-following procedure. The latter must be sophisticated and include techniques such as “line searches” and arc-length procedures [6, 7]. Initial flaws are not required, with initiation being governed by a strength criterion. Related work has been described by, among others, Schellekens and de Borst [8], Cui and Wisnom [9], Allix et al. [10], Mi et al. [11], Crisfield et al. [12], and Busso [17].

In the present article, we will apply two different interfacial decohesion laws to analyze a range of specimens that have been tested in the Department of Mechanical Engineering, Imperial College of Science, Technology and Medicine [13]. These are the double-cantilever beam (DCB), the end-load split (ELS), and the fixed-ratio mixed-mode (FRMM) specimens.

INTERFACE ELEMENTS

Although it is possible to use interface elements for three-dimensional analysis, the present study is concerned with two-dimensional plane-strain conditions. In these circumstances, the interface elements are effectively line elements as illustrated in Figure 1. The geometric thicknesses of the interface elements (Figure 1) are zero. However, they can be envisaged as having a finite effective thickness which is very small, so that the initial overall stiffness of the interface is very high. For simplicity, we will start by describing the simplest linear, four-node elements, which is illustrated in Figure 1a. We will also assume that the element lies in the “global x direction.” In reality this will often not be the case, and we must apply the usual transformations from local to global coordinates.

The “stress/strain” variables for the interface elements are the tractions and the relative displacements between the structural components at the interface. Nodes 3 and 4 in Figure 1a are on the top side, while nodes 1 and 2 are on the bottom side of the interface. Each node has two degrees of freedom, u and v . Thus a four-noded interface element has 8 displacement degrees of freedom, \mathbf{p} , where

$$\mathbf{p}^T = (v_1 \quad u_1 \quad v_2 \quad u_2 \quad v_3 \quad u_3 \quad v_4 \quad u_4) = [\mathbf{p}_{\text{bot}}^T, \mathbf{p}_{\text{top}}^T] \quad (1)$$

By subdividing \mathbf{p} into a set of degrees of freedom for the top and bottom surfaces,

$$\left. \begin{aligned} \mathbf{p}_{\text{bot}}^T &= (v_1 \quad u_1 \quad v_2 \quad u_2) \\ \mathbf{p}_{\text{top}}^T &= (v_3 \quad u_3 \quad v_4 \quad u_4) \end{aligned} \right\} \quad (2)$$

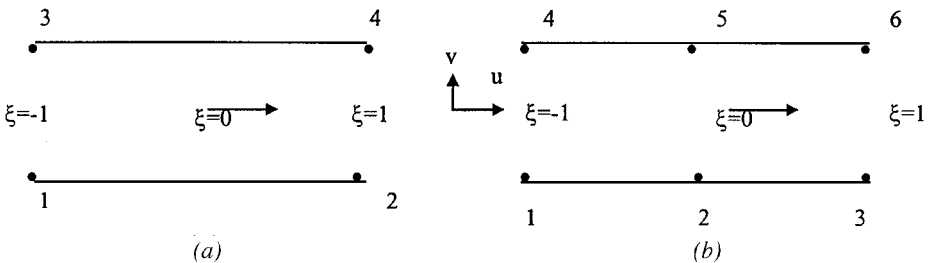


Figure 1. (a) Linear interface element. (b) Quadratic interface element.

the corresponding displacement fields, $\mathbf{u}^T = (v, u)$ would then be as follows (the order is v, u because of later use of mode I, mode II):

$$\begin{aligned}\mathbf{u}_{\text{bot}} &= \mathbf{H}\mathbf{p}_{\text{bot}} \\ \mathbf{u}_{\text{top}} &= \mathbf{H}\mathbf{p}_{\text{top}}\end{aligned}\quad (3)$$

where \mathbf{H} is the shape function matrix, with submatrices

$$\mathbf{H}_i = \begin{bmatrix} h_i & 0 \\ 0 & h_i \end{bmatrix} \quad (4)$$

The shape functions h_i are given as

$$\left. \begin{aligned} h_i &= -\frac{1}{2}(\xi - 1) & i &= 1, 3 \\ h_i &= \frac{1}{2}(\xi + 1) & i &= 2, 4 \end{aligned} \right\} \quad (5)$$

where ξ is the isoparametric coordinate of the interface element that is shown in Figure 1. Now we define the relative (strain-producing) displacements as the difference in displacements between the top and bottom surfaces:

$$\boldsymbol{\varepsilon} = \begin{Bmatrix} \varepsilon_{\text{I}} \\ \varepsilon_{\text{II}} \end{Bmatrix} = \mathbf{u}_{\text{top}} - \mathbf{u}_{\text{bot}} = \mathbf{H}\mathbf{p}_{\text{top}} - \mathbf{H}\mathbf{p}_{\text{bot}} = \mathbf{B}\mathbf{p} \quad (6)$$

where it should be noted that $\boldsymbol{\varepsilon}$ defines a set of relative displacements, not strains. As a shorthand, we will sometimes refer to them as “strains” but will always supply the inverted commas.

We now use virtual work to compute the internal nodal forces, \mathbf{q} , corresponding to the nodal displacements, \mathbf{p} , via

$$\mathbf{q} = \int_A \mathbf{B}^T \boldsymbol{\sigma} dA = \int_{-1}^1 \mathbf{B}^T \boldsymbol{\sigma} t a d\xi \quad (7)$$

where $\boldsymbol{\sigma}$ are the tractions (or pseudo-stresses), which are computed from the relative displacements in a manner that will be described shortly, while t is the thickness and a is the half-length of the element. The tangent stiffness relationships follow as

$$\delta \mathbf{q} = \mathbf{K}_t \delta \mathbf{p} \quad (8)$$

where

$$\mathbf{K}_t = \int_A \mathbf{B}^T \mathbf{D}_t \mathbf{B} dA = \int_{-1}^1 \mathbf{B}^T \mathbf{D}_t \mathbf{B} t a d\xi \quad (9)$$

We have so far described the simple linear interface element of Figure 1a. For analyses with LUSAS, we can also use a quadratic interface element, which is illustrated in Figure 1b. For both the linear and the quadratic elements, we integrate the internal forces and tangent stiffness matrices using Newton-Cotes rules. For the linear element this is a two-point procedure, so that we have a trapezoidal rule, while for the quadratic element we use a

three-point (they coincide with the nodes) integration rule. It is worth noting that attempts to use a two-point Gauss rule for the quadratic interface element will result in severe traction oscillations. Also, when combining the quadratic interface elements with eight-node “parent elements,” it is essential to use 3×3 rather than 2×2 Gaussian integration for the latter.

INTERFACIAL DECOHESION MODEL

We will start by describing the “material model” used in LUSAS and described in [11, 12]. For a simple mode I behavior, the input stress/“strain” relationship is that illustrated in Figure 2. It is defined by the interfacial tensile strength, σ_t , the cracking “strain,” ε_0 , and the maximum “strain,” ε_c . In the finite-element simulations, the “strain” can exceed ε_c , but the equivalent stress is then zero; that is, the interface is fully debonded. The elements where softening (such as fiber bridge or matrix ductility) take place are in the region $\varepsilon_0 < \varepsilon < \varepsilon_c$. In relation to Figure 2, the opening “strain” ε_c is chosen so that the area under the curve is equal to the critical fracture energy G_c , which is a material property. In practice, the adopted value of ε_0 is very small and $\varepsilon_c = 2G_c/\sigma_t$.

In order to define the interfacial behavior completely, we must specify the unloading response. For this interface element, a simple elastic damage model has been adopted so that, with reversing strains, the material is assumed to unload directly toward the origin. When combined with the proposed criterion for mixed-mode delamination, the resulting damage formulation leads to a very simple numerical algorithm [11, 12].

If we consider an individual interfacial location and subject it to increasing tensile strain increments, it is easy to show that

$$G_c = \int_0^{\varepsilon_c} \sigma \, d\varepsilon \tag{10}$$

so that once the traction has been reduced to zero, the fracture energy has been consumed. For simple mode I or mode II behavior, the user-supplied formulation used with ABAQUS

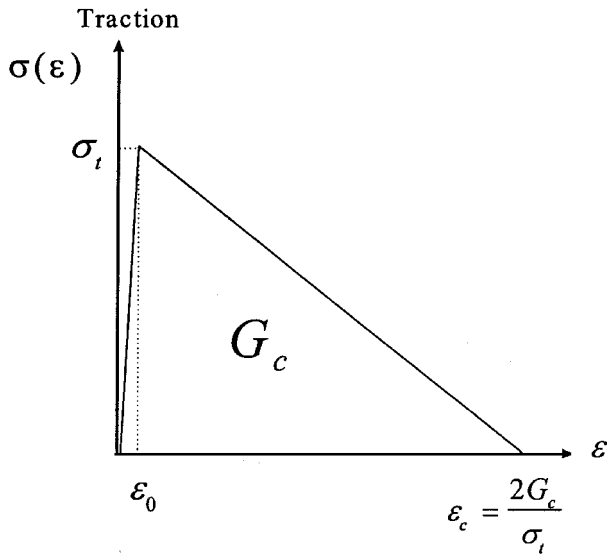


Figure 2. Linear interfacial decohesion model.

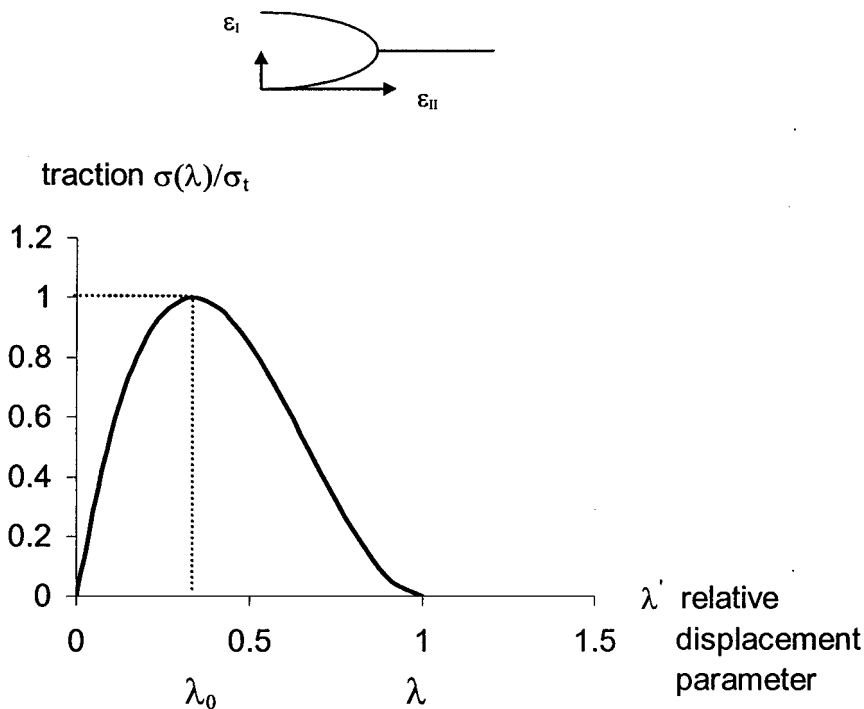


Figure 3. Cubic polynomial interfacial decohesion model and relative displacements.

is very similar (Figure 3) but replaces the simple bilinear relationship of Figure 2 with a cubic polynomial relationship.

For pure mode II behavior the adopted models are essentially the same, although now with the enclosed areas giving G_{IIc} and not G_{Ic} . Considering the interaction between mode I and mode II, analysts often use a linear interaction relationship that is given by Wu and Reuter [14]:

$$f_L = \frac{G_I}{G_{Ic}} + \frac{G_{II}}{G_{IIc}} = 1 \quad (11)$$

Experimental results indicate that a significant number of results lie between the previous linear relationship and a quadratic relationship given by

$$f_Q = \left(\frac{G_I}{G_{Ic}} \right)^2 + \left(\frac{G_{II}}{G_{IIc}} \right)^2 = 1 \quad (12)$$

Substituting Eq. (10) into Eq. (11) gives

$$f_L = \frac{\int \sigma_I d\varepsilon_I}{G_{Ic}} + \frac{\int \sigma_{II} d\varepsilon_{II}}{G_{IIc}} \quad (13)$$

With view to the satisfaction of Eq. (12), Mi et al. [11] and Crisfield et al. [12] proposed a “damage model” whereby, in place of the usual “scalar damage” relationship,

$\sigma = (1 - d)E_0\varepsilon$, they wrote

$$\sigma = \begin{Bmatrix} \sigma_I \\ \sigma_{II} \end{Bmatrix} = [\mathbf{I} - \mathbf{D}]\mathbf{E}_0 \begin{Bmatrix} \varepsilon_I \\ \varepsilon_{II} \end{Bmatrix} = \left[\mathbf{I} - \frac{\kappa}{1 + \kappa} \mathbf{F} \right] \mathbf{E}_0 \varepsilon \quad (14)$$

In Eq. (14), \mathbf{E}_0 is a diagonal matrix containing the initial stiffnesses in modes I and II, respectively, while \mathbf{F} is another diagonal matrix with diagonal entries given by

$$F_{ii} = \left[\frac{\varepsilon_c}{\varepsilon_c - \varepsilon_0} \right]_{i=I,II} \quad (15)$$

and κ is a scalar to be chosen, depending on the interaction model. In mode II, the terms ε_0 and ε_c are chosen in precisely the same manner as previously described for mode I, although now with $i = II$ in Eq. (15). We obtain the area under curve as G_{IIc} , so that $[\varepsilon_c]_{II} = [2G_c/\sigma_t]_{II}$. In the following, we will set $\varepsilon_{0I} = \varepsilon_{0II}$ and will define the scalar κ in Eq. (14) as

$$\kappa = [\varepsilon^T \mathbf{A} \varepsilon]^{1/2} - 1 \quad (16)$$

$$\mathbf{A} = \begin{bmatrix} \frac{1}{\varepsilon_{0I}^2} & 0 \\ 0 & \frac{1}{\varepsilon_{0II}^2} \end{bmatrix} \quad (17)$$

The term D_{ii} in (14) is not allowed to exceed unity. It can be shown that for monotonic straining, the application of (14)–(17) will recover (13). In order to generalize the method to recover Eq. (12), we rewrite Eq. (16) as

$$\kappa = \left[\left(\frac{\varepsilon_I}{\varepsilon_{0I}} \right)^\alpha + \left(\frac{\varepsilon_{II}}{\varepsilon_{0II}} \right)^\alpha \right]^{1/\alpha} - 1 \quad (18)$$

which coincides with (16) and (17) when α is set to 2. It can be shown [11, 12] that when α is set to 4, for monotonic straining, we recover (12). In most of the current applications, we have set α to 2.

In the absence of additional experimental information regarding unloading, it is simplest to introduce a basic “elastic damage model” whereby the unloading occurs linearly through the origin. To embed the material model within a conventional nonlinear finite-element program, we require the tangent modular matrix, \mathbf{D}_t , which is obtained from the variation of Eq. (14). This process leads to the relationship

$$\delta\sigma = \mathbf{D}_t \delta\varepsilon = \left[\left[\mathbf{I} - \frac{\kappa}{1 + \kappa} \mathbf{F} \right] \mathbf{E}_0 - \frac{1}{(1 + \kappa)^3} \mathbf{F} \mathbf{E}_0 \varepsilon \varepsilon^T \mathbf{A} \right] \delta\varepsilon \quad (19)$$

For the general case, the tangent modular matrix, \mathbf{D}_t , is nonsymmetric.

When using ABAQUS, for the equivalent mixed-mode formulation, we have adopted a model described by Busso [17]. As before, ε_I and ε_{II} are the normal and tangential components of the relative displacement across the interface location where the fracture process is

occurring, as indicated in Figure 3. Let ε_I^c and ε_{II}^c be the critical values of these displacement components, and define a single nondimensional separation measure as [18, 19]

$$\lambda = \sqrt{\left(\frac{\varepsilon_I}{\varepsilon_I^c}\right)^2 + \left(\frac{\varepsilon_{II}}{\varepsilon_{II}^c}\right)^2} \quad (20)$$

such that the tractions drop to zero when $\lambda = 1$. This relationship is closely linked to the earlier equation (16). The potential or fracture energy corresponding to the adopted σ , λ relationship is defined as

$$G_c = \varepsilon_I^c \int_0^1 \sigma(\lambda') d\lambda' \quad (21)$$

The normal and tangential components of the traction acting on the interface in the fracture process zone are given by

$$\sigma_I = \frac{\partial G_c}{\partial \varepsilon_I} = \frac{\sigma(\lambda)}{\lambda} \frac{\varepsilon_I}{\varepsilon_I^c} \quad \sigma_{II} = \frac{\partial G_c}{\partial \varepsilon_{II}} = \frac{\sigma(\lambda)}{\lambda} \frac{\varepsilon_I^c}{\varepsilon_{II}^c} \frac{\varepsilon_{II}}{\varepsilon_{II}^c} \quad (22)$$

Under a mode I response ($\varepsilon_{II} = 0$), Eq. (22) gives $\sigma_I = \sigma(\lambda)$, where $\lambda = \varepsilon_I / \varepsilon_I^c$. Under mode II ($\varepsilon_I = 0$), this equation gives $\sigma_{II} = \sigma(\lambda) \varepsilon_I^c / \varepsilon_{II}^c$, where $\lambda = \varepsilon_{II} / \varepsilon_{II}^c$. σ_t is the interfacial strength under pure mode I and under mode II it is $(\varepsilon_I^c / \varepsilon_{II}^c) \sigma_t$. In this work, it is conveniently assumed that $\varepsilon_I^c = \varepsilon_{II}^c$.

There is an important difference between this and the earlier model. The current is effectively, governed by a total critical fracture energy, G_c . In contrast, the earlier model relies on pure mode I and mode II fracture energy, G_{Ic} and G_{IIc} (from which ε_I^c and ε_{II}^c are obtained), which are input material parameters obtained from mode I and mode II tests. It should be noted that, in general, $G_c \neq G_{Ic} + G_{IIc}$. (Further discussion about this matter will be given in the section on FRMM specimens). It should be noted that the current model (with $\varepsilon_I^c = \varepsilon_{II}^c$) leads to a symmetric tangent modular matrix.

APPLICATIONS

For the analyses, we initially used linear elements for ABAQUS and quadratic elements for LUSAS. The respective meshes were such that we had roughly the same number of nodes in each case. As will be discussed later, the numerical results indicated a faster convergence rate with the linear elements and hence we later reanalyzed some of the examples in LUSAS using linear elements. In each case, when using linear elements, for the “parent elements,” we adopted an “enhanced strain formulation” [22], which gives almost the same performance as quadratic elements for many problems.

Numerical simulation of the double cantilever beam test

The loading and dimensions for the DCB specimen are illustrated in Figure 4. For the numerical simulations, displacement control is applied in conjunction with the “line search approach” in ABAQUS, while for LUSAS in some cases we used this solution procedure and in other cases we used a modified [6, 7] “cylindrical arc-length method.” In relation to

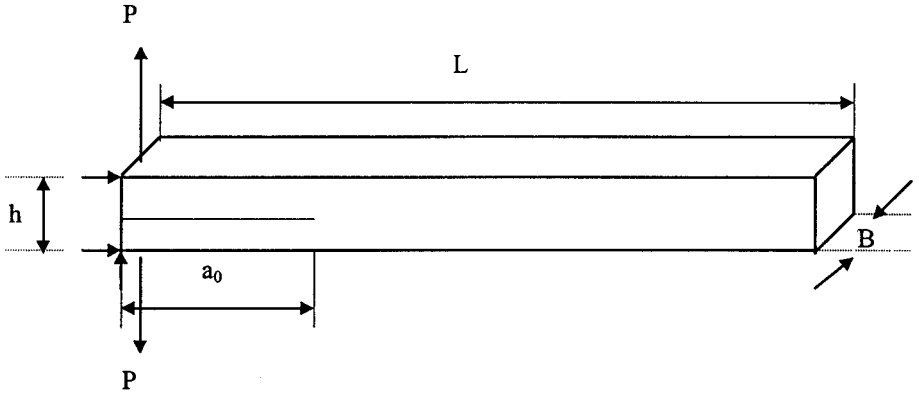


Figure 4. DCB boundary conditions for the beam.

Figure 4, the following dimensions and properties have been assumed for the beam material [13–15]:

$$\begin{aligned} L &= 150 \text{ mm} & B &= 24 \text{ mm} & h &= 3.1 \text{ mm} & a_0 &= 22 \text{ mm} \\ E_{11} &= 130 \text{ GPa} & E_{22} &= 8 \text{ GPa} & G_{12} &= 6 \text{ GPa} & \nu &= 0.27 \end{aligned}$$

where B , a_0 are the width of the beam and initial crack length, respectively. For the properties associated with the debonding interface, we have used

$$G_{Ic} = 0.257 \text{ N/mm} \quad \sigma_t = 48 \text{ N/mm}^2 \quad \varepsilon_0 = 1\text{E-}6$$

The interface elements are located along the growth direction from the tip of the initial crack to the other end of specimen. For the analyses, a relatively fine mesh was adopted with 8×600 linear elements for ABAQUS and 4×300 quadratic elements for LUSAS. Automatic solution procedures were adopted that led to relatively small displacement increments (see Figure 5).

The comparison among the experimental, analytical, and numerical load/deflection relationships is given in Figure 5. It can be seen that the overall load/deflection solution, obtained by the finite-element methods, is in close agreement with the experimental results. When using the linear element in ABAQUS and the quadratic element in LUSAS, it was found to be impossible to obtain a converged solution when the initial interlayer tensile strength of $\sigma_t = 48 \text{ N/mm}^2$ was adopted. As discussed in more detail in [11, 12], one way of overcoming these difficulties is to artificially reduce σ_t while preserving G_c . For a given G_c , the lower is σ_t , the easier is the convergence procedure, and the current example is particularly difficulty as it has a low G_c and high σ_t . When σ_t was reduced to 20 N/mm^2 in ABAQUS and 5 N/mm^2 in LUSAS, the convergence difficulties were overcome. This reduction did lead to some differences in the behavior around the peak load, but had little effect on the overall propagating response. A later analysis with LUSAS using linear elements with $\sigma_t = 20 \text{ N/mm}^2$ gave almost identical results to those obtained by ABAQUS. It is worth emphasizing that the first “cracking” (or attainment of σ_t) occurs much earlier than the peak load and, in relation to Figure 5, at about 20% of the peak load.

In order to provide a framework for the numerical simulations, we have also plotted in Figure 5 a closed-form solution based on a corrected beam theory [14, 23], which provides relationships among the load, the displacement, and the evolving crack length. However,

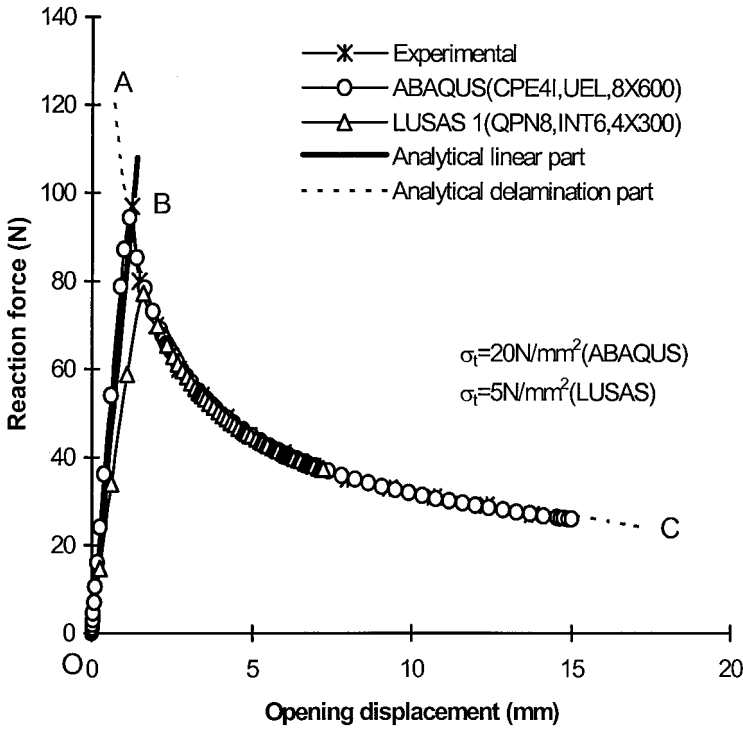


Figure 5. Load/displacement response for DCB.

for the current analyses, our primary concern is the relationship between the load and the displacement at the loading points (as plotted in Figure 5). To this end, we first obtain the load/deflection relationship (*OB*) for the initial crack length, a_0 , using corrected beam theory for a cantilever so that

$$\Delta = \frac{2P(a_0 + \chi h)^3}{3EI} \quad (23)$$

where I is the second moment of area of one arm of the cantilever and χ is a correction factor related to “root rotation” [14, 23]. To obtain the falling curve *ABC* in Figure 5, we simply set the energy release rate, $G = P^2(a + \chi h)^2/BEI$, to its critical value and hence eliminate the effective crack length, $a + \chi h$, to obtain

$$\Delta = \frac{2(BEIG_{1c})^{3/2}}{3EIP^2} \quad (24)$$

Clearly, the rising curve *OB* [from Eq. (23)], followed by the following curve *BC* [from Eq. (24)] gives a good approximation to both the finite-element and the experimental results. (There is a slight inconsistency in that the corrected beam theory solutions assume plane stress in the thickness direction while the finite-element results assume plane strain. However, the resulting differences can be shown to be small.) Closed-form solutions of the form of (24) have been given by Allix et al. [10] and Mi et al. [11], with the latter work also considering mode II and mixed-mode solutions relating to the experimental setup of Reeder

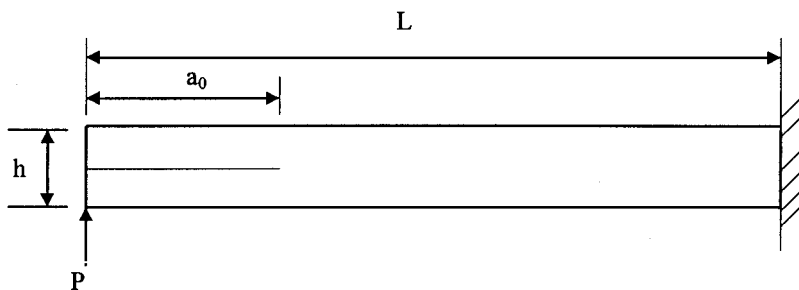


Figure 6. ELS boundary conditions for the beam.

and Crews [20]. These earlier solutions used simple beam theory rather than corrected beam theory.

Numerical simulation of the end-loading split test (ELS)

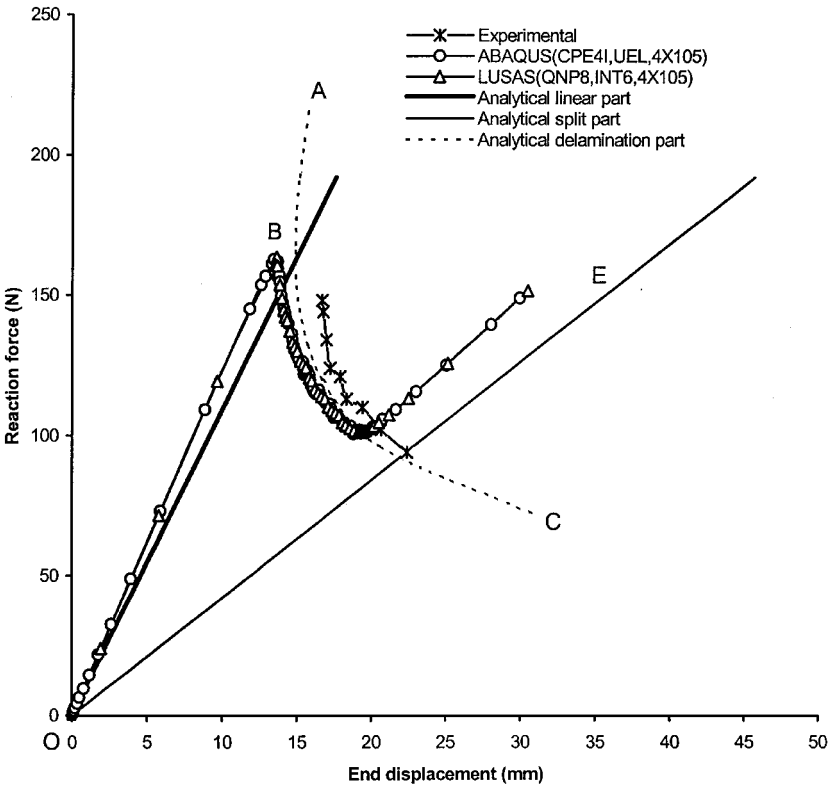
For this mode II analysis, we will simulate the experimental work of Blackman et al. [13, 15] and Kinloch et al. [14, 23], which is illustrated in Figure 6. In order to provide a framework for the numerical simulations, we again consider a set of closed-form solutions based on corrected beam theory. The closed-form corrected beam theory solutions are derived in the Appendix. In relation to Figure 7a, we have three “curves.” The first relationship, *OB*, is the loading line associated with a particular initial length of crack, a_0 . The second curve, *ABC*, is the propagating delamination part, for which we again set the energy release rate to its critical value. The third solution (*OE*) is governed by the stiffness of the complete split beam (see Appendix).

The dimensions and properties used for the numerical simulation of Figure 7a were

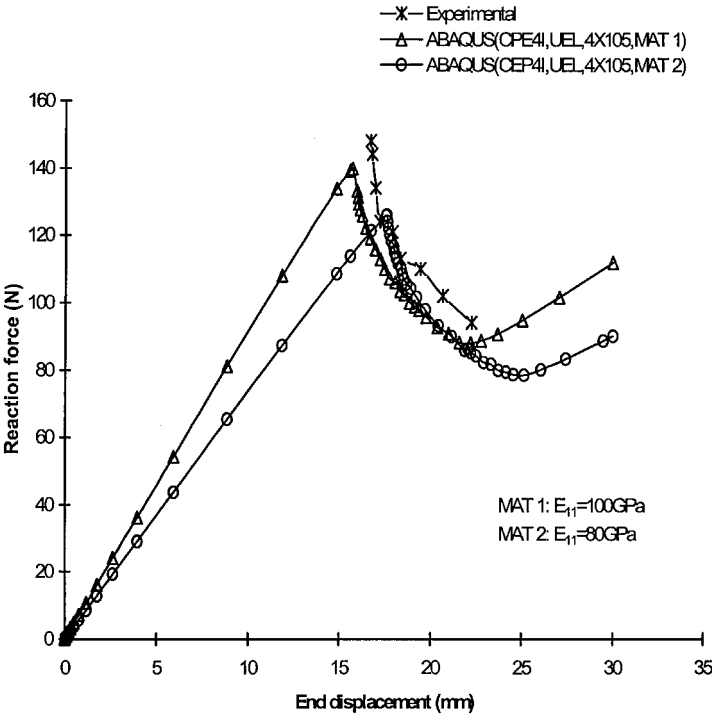
$$\begin{aligned}
 L &= 105 \text{ mm} & B &= 24 \text{ mm} & h &= 3.05 \text{ mm} & a_0 &= 60 \text{ mm} \\
 E_{11} &= 130 \text{ GPa} & E_{22} &= 8 \text{ GPa} & \nu &= 0.27 & G_{12} &= 6 \text{ GPa} \\
 G_{IIc} &= 0.856 \text{ N/mm} & \sigma_t &= 48 \text{ N/mm}^2 & \varepsilon_0 &= 1\text{E-}6
 \end{aligned}$$

For ABAQUS a 4×105 mesh of linear elements was adopted, while for LUSAS a mesh of 4×105 quadratic elements was initially adopted. The adopted boundary conditions are slightly different from those provided in the experiment. In order to avoid large deflection effects, the specimen is free to move in the horizontal direction. However, for the finite-element simulations, we do not need to introduce this boundary condition, because we simply “switch off” large-deflection effects.

There is a close agreement between the two sets of finite-element results and a reasonable agreement with the analytical solution. However, the experimental results are in poor agreement with the initial finite-element slope. This could be due to the complex loading and boundary conditions in the real test. To overcome this we use two modified material E_{11} values (see Figure 7b) to reanalyze the problem. The solution with $E_{11} = 100$ GPa gives good agreement with the initial slope, while the solution with $E_{11} = 80$ GPa gives better agreement with experimental results in the propagating delamination region. In both cases the reduction (from the normal value of 130 GPa) could be consistent with an incorrect flexibility associated with “gripping” problems. It is noted that only ABAQUS was used for this analysis, because we have already shown the close agreement between the two finite-element procedures in Figure 7a.



(a)



(b)

Figure 7. Load/displacement responses for ELS.

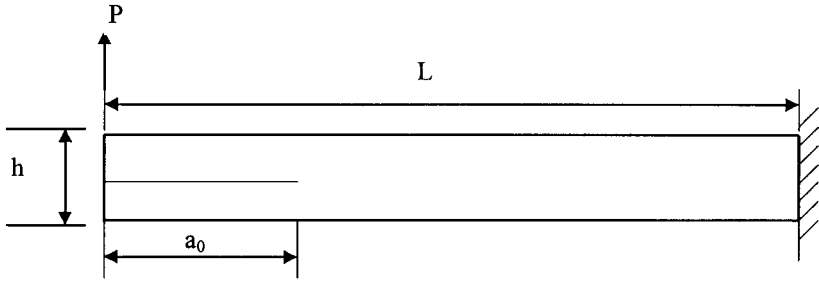


Figure 8. FRMM boundary conditions for the beam.

Numerical simulation of the fixed-ratio mixed-mode (FRMM) test

Figure 8 shows the FRMM specimen, which has the following dimensions and properties [13–15]:

$$\begin{aligned}
 L &= 105 \text{ mm} & B &= 24 \text{ mm} & h &= 3.1 \text{ mm} & a_0 &= 45 \text{ mm} \\
 E_{11} &= 130 \text{ GPa} & E_{22} &= 8 \text{ GPa} & \nu &= 0.27 & G_{12} &= 6 \text{ GPa} \\
 G_c \text{ (total)} &= 0.434 \text{ N/mm} & \sigma_t &= 48 \text{ N/mm}^2 & \varepsilon_0 &= 1\text{E-}6
 \end{aligned}$$

Using ABAQUS with linear elements, the adopted mesh was 8×420 , while for LUSAS with quadratic elements the mesh was 4×210 . As with the earlier ELS, we again used the removal of large-deflection effects, to simplify the boundary conditions.

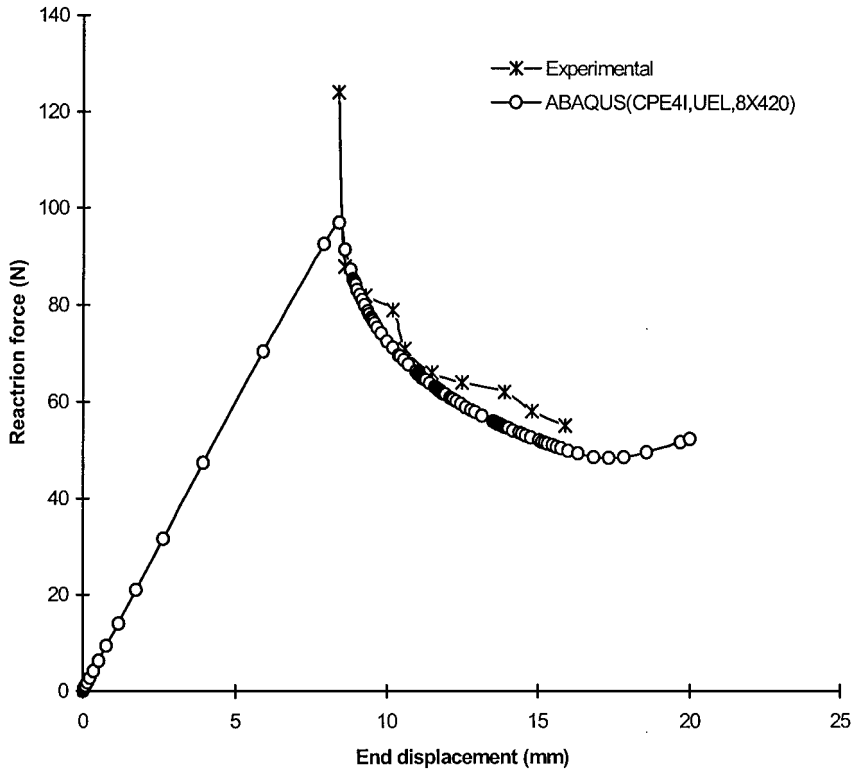
Figure 9a compares the experimental results [13–15] with the finite-element solutions and those obtained by corrected beam theory (details in the Appendix). From Figure 9a, the results with $E_{11} = 130 \text{ GPa}$ give good agreement within the delamination region, although the initial slope is too low. To overcome this, we increased the E_{11} value to get a better correlation with the initial slope (see Figure 9b). However, in contrast to the ELS specimen, for which a physical explanation could be found for reducing the E value, we cannot suggest a physical reason for this increase.

For this case, the G_c value given earlier is the total energy obtained under the process described in [14, 23]. As already discussed, this is the value required for the interfacial decohesion model used in ABAQUS. In order to obtain an equivalent solution with LUSAS, we artificially input $G_{Ic} = G_{IIc} = G_c \text{ (total)}$, so that Eq. (11) effectively gives $G_I + G_{II} = G_c$, which is equivalent to the formulation adopted in our ABAQUS interface model. The close agreement between the two finite-element solutions can be seen from Figure 9b.

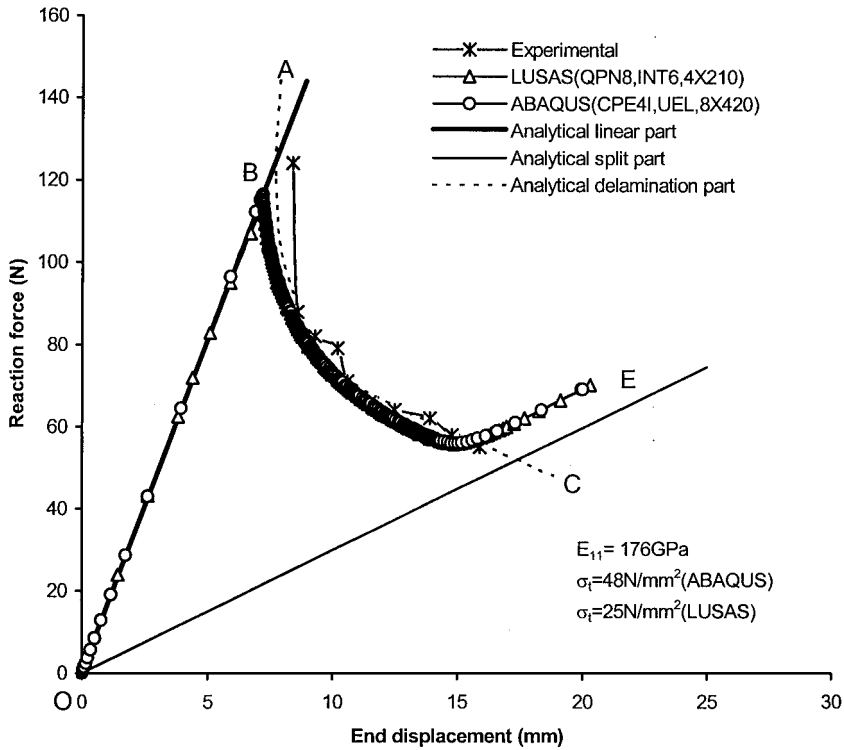
Now we use the LUSAS interface model as originally intended by directly inputting the pure G_{Ic} and G_{IIc} values (as obtained from DCB and ELS specimens directly). From previous applications the pure G_{Ic} and G_{IIc} are 0.257 and 0.856, respectively. Assuming the total fracture $G_c \text{ (total)}$ is simply obtained as

$$G_I + G_{II} = G_c \quad (25)$$

and knowing $G_I = \frac{4}{3}G_{II}$, we can use Eq. (11) to obtain $G_c = 0.367$, which is lower than the value of 0.434 which we used in the earlier analysis. This is confirmed by the current LUSAS finite-element response obtained with $\alpha = 2$ [see Eq. (18)], which, from Figure 10, is much lower than the experimental solution. If we consider the quadratic interaction relationship in Eq. (12) and combine it with Eq. (25) and the relationship $G_I = \frac{4}{3}G_{II}$, the total energy G_c rises to 0.438, which is very close to the earlier 0.434. This is confirmed



(a)



(b)

Figure 9. Load/displacement responses for FRMM.

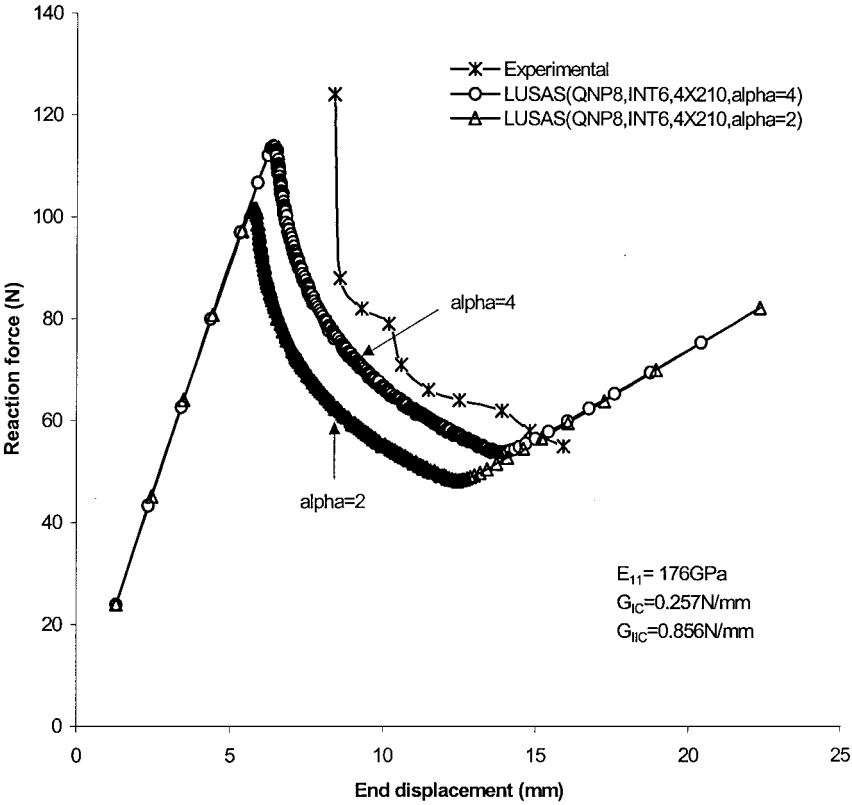


Figure 10. Load/displacement response for FRMM.

by the current LUSAS finite-element formulations obtained with $\alpha = 4$ (see Figure 10), which are in reasonable agreement with the earlier results. This is illustrated in Figure 10, which shows that the response obtained with $\alpha = 4$ is much better than that obtained with $\alpha = 2$.

Additional numerical tests

It was mentioned earlier that when using LUSAS with quadratic elements, the convergence behavior was found to be significantly worse than that obtained using ABAQUS with linear elements. In particular, to obtain a converged solution for the DCB test, it was necessary to reduce the interfacial tensile strength, σ_t , to 5 N/mm² when using quadratic elements. At this stage it was not clear whether or not this difference was an effect of the element types or of the adopted incremental/iterative solution procedures. To resolve this issue, we reanalyzed the DCB specimen in LUSAS (with a simple change of properties so that they were isotropic with $\sigma_t = 20$ N/mm²) using both the linear (a 8×600 mesh) interface elements and quadratic interface elements (a 4×300 mesh). In each case an automatic solution procedure was adopted, with the desired number of iterations being set to four. Up to an opening displacement of 10 mm (see Figure 11, in which the results from the upper curve are multiplied by a factor of 1.5 in order to allow us to distinguish between the two solutions), the number of iterations required for the quadratic elements was 90, while with the linear elements the convergence rate improved significantly, so that fewer than 50 increments were required.

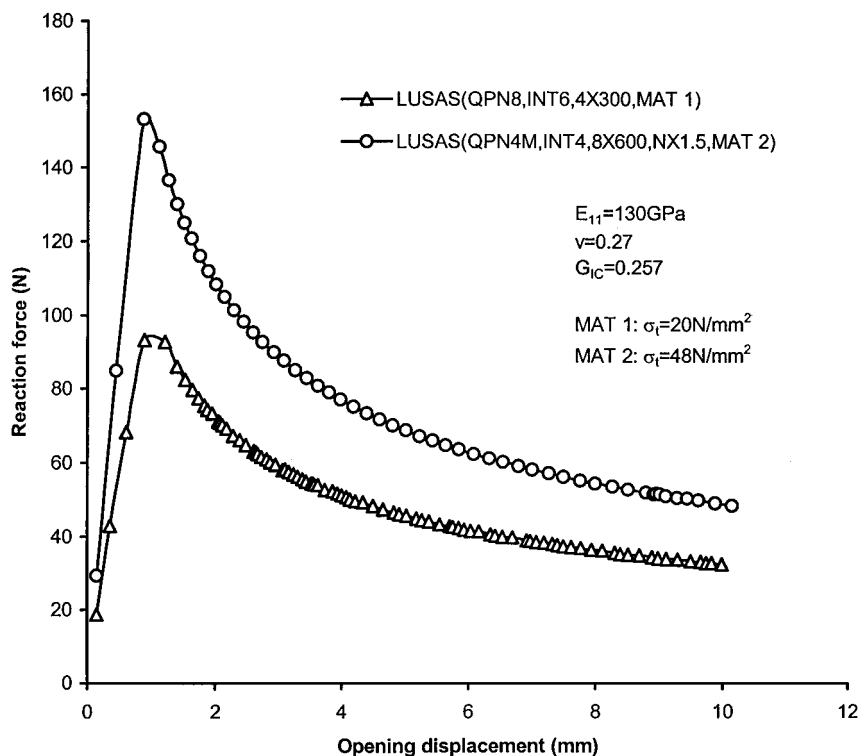


Figure 11. Load/displacement response for DCB.

CONCLUSIONS

This article has described the development and application of interface elements to the prediction of progressive delamination. The solutions have been compared with experimental results from composite material specimens. Two different but related interfacial decohesion models have been embedded within two different finite-element codes, and the computed results have been very similar and in close agreement with both the experimental results and solutions obtained from a corrected beam theory.

For comparison with both the ELS and to a lesser extent the FRMM specimens, the E values have had to be adjusted in order to obtain a close correlation. For some problems, it has been necessary to artificially reduce the cracking strains (while maintaining the critical fracture energies) in order to obtain convergence. The latter is significantly easier to achieve with linear elements than with quadratic elements.

REFERENCES

- [1] *ABAQUS User's Manual*, Hibbitt, Karlsson & Sorensen (UK), Cheshire, UK, 1996.
- [2] *LUSAS User's Manual*, FEA, Kingston-upon-Thames, UK, 1997.
- [3] E. F. Rybicki and M. F. Kanninen, A Finite Element Calculation of Stress Intensity Factors by a Modified Crack Closure Integral, *Eng. Fracture Mech.*, vol. 9, pp. 931–938, 1977.
- [4] I. S. Raju, Calculation of Strain-Energy Release Rate with Higher Order and Singular Elements, *Eng. Fracture Mech.*, vol. 28, pp. 251–274, 1987.
- [5] B. D. Davidson and R. A. Schapery, A Technique for Predicting Mode I Energy Release Rates Using a First-Order Shear Deformation Plate Theory, *Eng. Fracture Mech.*, vol. 36, pp. 157–165, 1990.

- [6] M. A. Crisfield, *Non-linear Finite Element Analysis of Solids and Structures, Vol. 1*, Wiley, Chichester, UK, 1991.
- [7] M. A. Crisfield, *Non-linear Finite Element Analysis of Solids and Structures, Vol. 2*, Wiley, Chichester, UK, 1997.
- [8] J. C. Schellekens and R. de Borst, Free Edge Delamination in Carbon Epoxy Laminates a Novel Numerical/Experimental Approach, *Composite Struct.*, vol. 28, pp. 467–474, 1993.
- [9] W. Cui and M. R. Wisnom, A Combined Stress-Based and Fracture-Mechanics-Based Model for Predicting Delamination in Composites, *Composites*, vol. 6, pp. 467–474, 1993.
- [10] O. Allix, P. Ladeveze, and A. Corigliano, Damage Analysis of Interlaminar Fracture Specimens, *Composite Struct.*, vol. 31, pp. 61–74, 1995.
- [11] Y. Mi, M. A. Crisfield, H.-B. Hellweg, and G. A. O. Davies, Progressive Delamination Using Interface Elements, *J. Composite Mater.*, vol. 32, pp. 1246–1272, 1998.
- [12] M. A. Crisfield, Y. Mi, G. A. O. Davies, and H.-B. Hellweg, Finite Element Method and the Progressive Failure Modelling of Composite Structures, in D. R. J. Owen, E. Hinton, E. Oñate (eds.), *CIMNE, Computational Plasticity: Fundamentals & Applications*, part 1, pp. 239–254, Barcelona, 1997.
- [13] B. R. K. Blackman, Imperial College Results from an ESIS TC4 Round-Robin on Interlaminar Fracture Toughness Testing (7th Round Robin), 1994.
- [14] A. J. Kinloch, Y. Wang, J. G. Williams, and P. Yayla, The Mixed-Mode Delamination of Fibre Composite Materials, *Composite Sci. Technol.*, vol. 47, pp. 225–237, 1993.
- [15] B. R. K. Blackman, J. P. Dear, A. J. Kinloch, H. MacGillivray, Y. Wang, J. G. Williams, and P. Yayla, The Failure of Fibre Composites and Adhesively Bonded Fibre Composites under High Rates of Test, *J. Mater. Sci.*, vol. 31, pp. 4467–4477, 1996.
- [16] E. M. Wu and R. C. Reuter, Jr., Crack Extension in Fibreglass Reinforced Plastics, Rep. 275, T & AM, University of Illinois, 1965.
- [17] E. P. Busso, Fracture Resistance of Glass and Polymer Bonded Si-Wafer Systems Used in Microsensor Devices, submitted, 1989.
- [18] V. Tvergaard and J. W. Hutchinson, The Influence of Plasticity on Mixed Mode Interface Toughness, *J. Mech. Phys. Solids*, vol. 41, pp. 1119–1135, 1993.
- [19] V. Tvergaard and J. W. Hutchinson, Toughness of an Interface along a Thin Ducline Layer Join Elastic Solids, *Phil. Mag. A*, vol. 70, pp. 641–656, 1994.
- [20] J. R. Reeder and J. H. Crews, Mixed-Mode Bending Method for Delamination Testing, *AIAA J.*, vol. 28, pp. 1270–1276, 1990.
- [21] Y. Mi and M. A. Crisfield, Relationship for the DCB and MMB and Proof of the FEA Formulation, Imperial College Rep., Department of Aeronautics, ISBN 0308-7247, 1997.
- [22] J. C. Simo and M. S. Rifai, A Class of Assumed Strain Methods and the Method of Incompatible Modes, *Int. J. Numer. Meth. Eng.*, vol. 29, pp. 1959–1638, 1990.
- [23] S. Hashemi, A. J. Kinloch, and J. G. Williams, The Analysis of Interlaminar Fracture in Uniaxial Fibre-Polymer Composite, *Proc. Roy. Soc. Lond.*, vol. A427, pp. 173–199, 1990.

APPENDIX: CLOSED-FORM SOLUTION FOR MODE II (ELS) AND MIXED-MODE (FRMM) DELAMINATION BY CORRECTED BEAM THEORY

ELS

In relation to Figure 7a, the initial loading line *OB* is given by

$$\Delta = \frac{P \left[(L + \chi_I h)^3 + 3(a_0 + \chi_{II} h)^3 \right]}{3EI_F} \quad (A1)$$

where χ_I and χ_{II} are the corrected factors for simple beam theory [11–13], L is the length

of the beam, and I_F is the second moment of area of the beam, which is given by

$$I_F = \frac{Bh^3}{12}$$

For the unloading line ABC , using $G = G_c = 3P^2a^2/2BEI_F$, we obtain

$$\Delta = \frac{P(L + \chi_I h)^3 + 3P(2BEI_F G_c / 3P^2)^{3/2}}{3EI_F} \quad (A2)$$

where G_c is the fracture energy of mode II. Finally, line OE of Figure 7a relates to the completely split beam, for which

$$\Delta = \frac{4P(L + \chi_I h)^3}{3EI_F} \quad (A3)$$

FRMM

Similarly, in relation to Figure 9b, the initial loading line OB is given by

$$\Delta = \frac{P[(L + \chi_I h)^3 + 7(a + \chi_{II} h)^3]}{3EI_F} \quad (A4)$$

For the unloading curve ABC , using $G_I + G_{II} = G_c = 7P^2a^2/2BEI_F$, we obtain

$$\Delta = \frac{P(L + \chi_I h)^3 + 7P(2BEI_F G_c / 7P^2)^{3/2}}{3EI_F} \quad (A5)$$

where G_c is the total fracture energy of mixed mode I/II. Again, the line OE of Figure 9b relates to the completely split beam, for which

$$\Delta = \frac{8P(L + \chi_I h)^3}{3EI_F} \quad (A6)$$